UCSF
UC San Francisco Previously Published Works

Title
A novel approach for integrative studies on neurodegenerative diseases in human brains

Permalink
https://escholarship.org/uc/item/3r1069vr

Authors
Theofilas, Panos
Polichiso, Livia
Wang, Xuehua
et al.

Publication Date
2014-04-01

DOI
10.1016/j.jneumeth.2014.01.030

Peer reviewed

eScholarship.org Powered by the California Digital Library
University of California

Journal of Neuroscience Methods 226 (2014) 171–183

Contents lists available at ScienceDirect

Journal of Neuroscience Methods

journal homepage: www.elsevier.com/locate/jneumeth

Basic Neuroscience

A novel approach for integrative studies on neurodegenerative diseases in human brains

Panos Theofilas[a,1], Livia Polichiso[a,b,1], Xuehua Wang[a], Luzia C. Lima[b,c], Ana T.L. Alho[b,c], Renata E.P. Leite[d], Claudia K. Suemoto[e], Carlos A. Pasqualucci[d], Wilson Jacob-filho[e], Helmut Heinsen[f], Lea T. Grinberg[a,b,*], Brazilian Aging Brain Study Group[d]

[a] Memory and Aging Center, Department of Neurology, University of California, San Francisco Nelson Rising Lane, P.O. Box 1207, San Francisco, CA 94143, USA
[b] Discipline of Pathophysiology, University of Sao Paulo Medical School, Av. Dr. Arnaldo 455, Sao Paulo, CEP 01246903, SP, Brazil
[c] Hospital Israelita Brasileiro Albert Einstein, Av. Albert Einstein 627/701, Sao Paulo, SP, Brazil
[d] Department of Pathology, LIM-22, University of Sao Paulo Medical School, Av. Dr. Arnaldo 455, sala 1353, Sao Paulo, CEP 01246903, SP, Brazil
[e] Division of Geriatrics, University of Sao Paulo Medical School, Av. Dr. Arnaldo 455, sala 1151, Sao Paulo, SP, Brazil
[f] Laboratory of Morphological Brain Research, Department of Psychiatry, University of Wuerzburg, Oberdürrbacher Str. 6, 97080 Würzburg, Germany

HIGHLIGHTS

- Network-based approach for studying differential vulnerability in neurodegeneration.
- Allow to combine stereology, immunohistochemistry and 3D reconstruction.
- Suitable for humans and animal models.
- The approach is economical and requires shorter processing and analysis time.
- This method can make studies with human brain tissue more attractive.

ARTICLE INFO

Article history:
Received 4 September 2012
Received in revised form
17 November 2013
Accepted 27 January 2014

Keywords:
Brainstem
Stereology
3D reconstruction
Neuropathology
Human
Immunohistochemistry
Brain network
Alzheimer's disease
Neurodegenerative diseases

ABSTRACT

Despite a massive research effort to elucidate Alzheimer's disease (AD) in recent decades, effective treatment remains elusive. This failure may relate to an oversimplification of the pathogenic processes underlying AD and also lack of understanding of AD progression during its long latent stages. Although evidence shows that the two specific neuropathological hallmarks in AD (neuronal loss and protein accumulation), which are opposite in nature, do not progress in parallel, the great majority of studies have focused on only one of these aspects. Furthermore, research focusing on single structures is likely to render an incomplete picture of AD pathogenesis because as AD involves complete brain networks, potential compensatory mechanisms within the network may ameliorate impairment of the system to a certain extent. Here, we describe an approach for enabling integrative analysis of the dual-nature lesions, simultaneously, in all components of one of the brain networks most vulnerable to AD. This approach is based on significant development of methods previously described mainly by our group that were optimized and complemented for this study. It combines unbiased stereology with immunohistochemistry and immunofluorescence, making use of advanced graphics computing for three-dimensional (3D) volume reconstructions. Although this study was performed in human brainstem and focused in AD, it may be applied to the study of any neurological disease characterized by dual-nature lesions, in humans and animal models. This approach does not require a high level of investment in new equipment and a significant number of specimens can be processed and analyzed within a funding cycle.

© 2014 Elsevier B.V. All rights reserved.

* Corresponding author at: University of California, San Francisco, 675 Nelson rising Lane, PO box 1207, 94158, USA. Tel.: +1 415 502 7229; fax: +1 415 476 5573.
E-mail address: Lea.Grinberg@ucsf.edu (L.T. Grinberg).
[1] These authors contributed equally to the manuscript.

0165-0270/$ – see front matter © 2014 Elsevier B.V. All rights reserved.
http://dx.doi.org/10.1016/j.jneumeth.2014.01.030

1. Introduction

The dramatic increase in life expectancy worldwide is being followed by an increase in the prevalence of Alzheimer's disease (AD), the leading cause of dementia (Hebert et al., 2003).

AD is characterized by two specific neuropathological hallmarks which are opposite in nature: (a) positive lesions caused by extracellular accumulation of β-amyloid peptides in neuritic plaques (NPs) and intracellular accumulation of phosphorylated tau protein in neurofibrillary tangles (NFTs) and (b) negative lesions (neuronal and synaptic loss) (Duyckaerts et al., 2009). Positive and negative AD lesions do not develop in parallel (Andrade-Moraes et al., 2013). Despite this complex pathogenesis, research effort has been directed to the elucidation of a limited number of candidate pathways involved in the positive lesions, such as the amyloid cascade (Korczyn, 2012). It may partly explain why a number of promising therapies for AD that appeared to have great efficacy in animal models fell short when tested in human AD subjects (Huang and Mucke, 2012). AD is associated with a highly characteristic spread pattern across specific neural networks (Seeley et al., 2009), accompanied by the activation of and/or damage to an increased number of cellular and molecular pathways. Studies show that potential compensation mechanisms among the components the vulnerable network ameliorate impairment of the system to a certain extent (Boxer et al., 2011), suggesting that research focusing on single structures is likely to render an incomplete picture of AD pathogenesis.

In 2009, using a postmortem brain collection including over 1500 controls (Grinberg et al., 2007), we demonstrated for the first time that a midbrain structure, the dorsal raphe nucleus, showed NFT pathology even before the entorhinal cortex, the structure previously considered to be the first affected by NFT. The dorsal raphe nucleus is part of the isodendritic core (IC) network, which also includes the cholinergic nucleus basalis of Meynert (NbM), the noradrenergic locus coeruleus and the dopaminergic substantia nigra (Ramon-Moliner and Nauta, 1966). These inter-connected nuclei share a similar neuron appearance when Golgi-stained, and modulate basic physiological processes and behavior. All IC components show AD changes during AD latent stage, years before the symptoms onset (Braak et al., 2011; Geula et al., 2008; Ohm et al., 1989; Parvizi et al., 2001; Sassin et al., 2000). Since AD treatment is likely to be more effective if started during its long latent stage (Jack et al., 2010), before a large percent of brain tissue has already been irrevocably damaged, studies on the IC during early AD is a top priority (Grinberg et al., 2009b).

With this vision, we aimed to take advantage of our large and ongoing postmortem brain collection to investigate IC involvement in early AD. However, aware of the complexities of AD pathogenesis, we aimed to develop an approach for enabling integrative analysis of the dual-nature AD lesions in all IC components simultaneously. This process was based on methods mainly described previously by our group (Ewers et al., 2011; Grinberg et al., 2008a, 2009a, c; Grinberg and Heinsen, 2007; Heinsen et al., 2000, 2004) that were optimized and complemented for this study. It combines unbiased stereology with immunohistochemistry and immunofluorescence, making use of advanced graphics computing for three-dimensional (3D) volume reconstructions.

2. Materials and methods

2.1. Subjects

Postmortem human brains from four subjects aged ≥50 years, with no cognitive decline (clinical dementia rating, CDR = 0) (Morris, 1993) or parkinsonism (Tanner et al., 1990) were supplied by the Brain Bank of the Brazilian Brain Aging Study Group (BBBABSG) (Grinberg et al., 2007; Table 1). All subjects showed latent AD (pathology was detected in the brains, but no clinical decline was present). After informed consent, clinical and functional information were obtained from knowledgeable informants who were interviewed by nurses specifically trained for the questionnaire application (Ferretti et al., 2010).

Table 1
Characteristics of cases.

Cases	Age (years)	Gender	Post-mortem interval (h)	Cause of death
1	69	Male	17	Hemopericardium
2	62	Male	17.5	Cachexia
3	59	Male	20	Myocardial infarction
4	56	Male	19.5	Broncopneumonia

2.2. Tissue processing

2.2.1. Initial brain processing

Brains were fixed by immersion in 8% paraformaldehyde for at least 4 weeks. The brainstem and thalamus were then severed from the brain as a unit and the cerebellum was removed to produce the brainstem block. A second block (basal forebrain block) was constituted of a 2 cm thick coronal brain slab encompassing the NbM. Both blocks were processed as described below.

For neuropathological assessment, specific brain areas were sampled according to the BBBABSG protocol (Grinberg et al., 2007).

2.2.2. Celloidin embedding

The brainstem and forebrain blocks were initially embedded in celloidin using the modified method developed by Heinsen et al. (2000). This method reduced tissue distortion and enabled production of thick histological sections, a requirement for the subsequent stereological studies. Prior to embedding, the meningeal and pial vessels were removed to reduce artifactual damage and the blocks were dehydrated in a graded series of ethanol solutions (70, 80, and 96% in dH_2O). The dehydrated blocks were then individually placed in glass boxes filled with 8% celloidin solution in 100% ethanol (Hacocell H 9 IPA 35%, Hagedorn, Osnabrück, Germany). We modified our original protocol by mixing 0.1% Sudan black B (Sigma–Aldrich, St. Louis, MO) in a proportion of 50:1 with celloidin aiming to improve the contrast between the tissue and the embedding media. To ensure proper embedding, the volume of celloidin was at least double the block volume and the block did not come into contact with the walls of the box. The glass boxes were individually placed in a desiccator connected to a vacuum pump with pressure set at −600 mb (−60 kPa) or −400 mb (−40 kPa) until the celloidin contracted to half its original volume, becoming clear and semi-solid (Fig. 1). Blocks were then placed in a covered aquarium which volume was 30 times greater than the block, together with a 1000 ml beaker filled with 200 ml chloroform. The chloroform vapor hardened the celloidin to an India rubber consistency by promoting alcohol removal from the block (Fig. 2).

2.2.3. Sectioning and imaging of the celloidin-embedded brain tissue blocks

Excess celloidin was trimmed off the blocks with a knife before mounting on a polyamide base that was later attached to a microtome (Fig. 2). The same 8% celloidin solution was used to glue the blocks into the base. Blocks remained in the aquarium overnight, followed by exposure to 70% ethanol for a minimum of 2 h to ensure that the celloidin blocks were firmly attached to the base. The blocks were sectioned at 300 μm thickness using either a

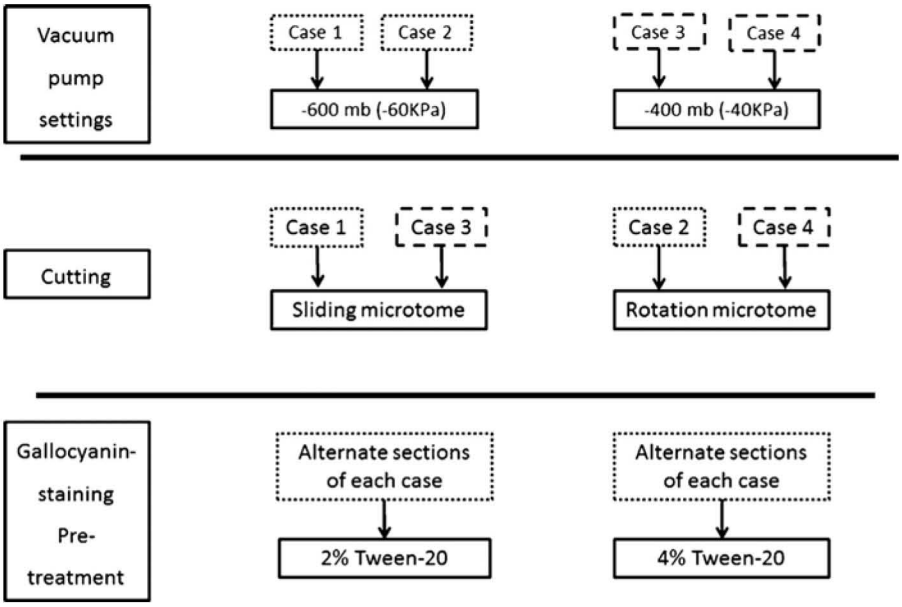

Fig. 1. Study design for optimizing the proposed approach.

rotation microtome (HM355S, Thermo Scientific, Waltham, MA, USA) or a sliding microtome (AO 880, American Optical, USA) (Figs. 1, 2C and D, and 3) and were immediately stored in 70% alcohol for further processing.

During block sectioning, a series of images were acquired directly from the block following each cut using a high definition DSR camera (EOS 5D Mark II, Canon, Tokyo, Japan) mounted on a copy stand arm (Kaiser Fototechnik, Germany) and linked to a computer (Fig. 3B).

2.2.4. Gallocyanine staining

Each section was numbered and all even-numbered sections were stained with gallocyanine, a progressive Nissl stain that does not require differentiation for removing excess dye. Sections were briefly rinsed in dH_2O and immersed in Tween-20 for 2 h. The Tween-20 step is a modification of the original protocol and was used to solubilize lipids and membrane proteins, thus facilitating staining and background clearing. Since overexposure to this detergent could compromise myelin, two different concentrations of

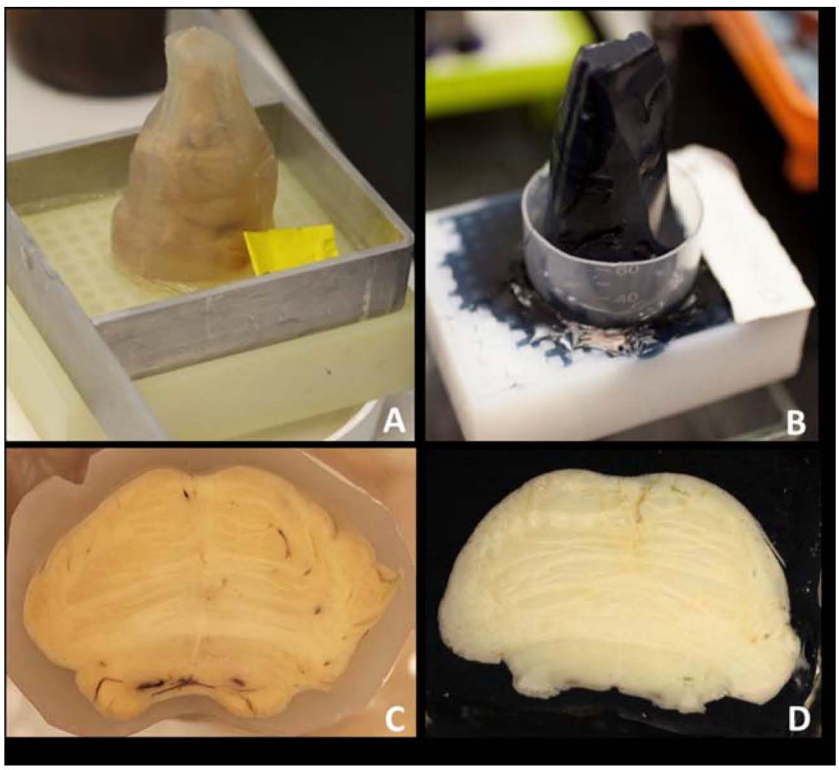

Fig. 2. Clear (A) or Sudan black B-stained celloidin (B) was used for brainstem embedding. Blocks were subsequently trimmed and attached on a plastic base, with the caudal end facing up. Brainstem borders of horizontal sections embedded in stained celloidin were much easier to identify compared to sections embedded in clear celloidin, and thus histological volume reconstruction could be completely automated using stained-celloidin embedding (C and D).

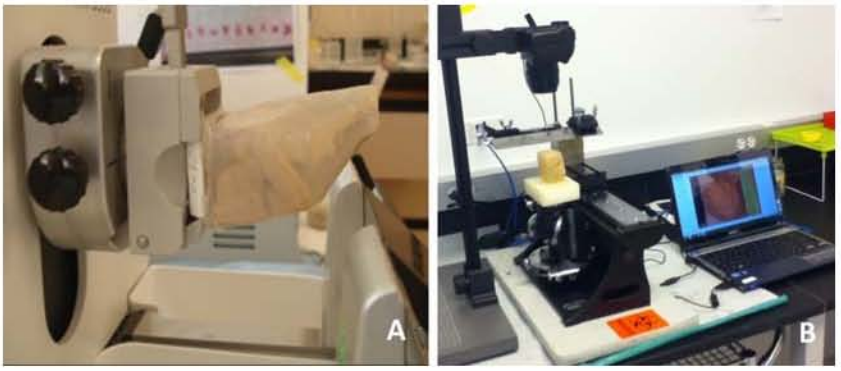

Fig. 3. Tissue sectioning and image acquisition: two types of equipment were used for tissue sectioning. These include a rotation microtome (A) and a sliding microtome (B). In both methods, a camera was mounted over the block for image acquisition. Both methods provided similar histological sections, however the sliding microtome cutting angle allowed for camera mounting without obstructing the operator.

Tween-20 (2% and 4%; protocols A and B, respectively) were tested (Fig. 1). After rinsing in tap water, the sections were incubated in performic acid (1 part of 100% formic acid, 3 parts of 30% H_2O_2, and 6 parts of dH_2O) overnight to remove the staining background, rinsed in tap water again and finally placed in gallocyanine–chromalum pH 1.8 (1.5 g gallocyanine (Acros organics, Geel, Belgium) in 1000 ml of 5% chromic potassium sulfate dodecahydrate (Merck, Darmstadt, Germany) for 2 h). A shaker set at low speed was used throughout to ensure uniform staining. After the staining, the sections were compressed between two filter papers and quenched between stainless steel perforated metal plates kept together by a metal clip to guarantee flatness during the dehydration step. Sections were mounted using permount medium (Thermo Scientific, Waltham, MA, USA) with 6% 1-bromonaphthalene (Sigma–Aldrich, St. Louis, MO, USA) and required a minimum of one month to dry.

2.2.5. Immunohistochemistry

Odd-numbered sections were reserved for immunohistochemistry. Two protocols were developed, one for thin sections – intended for providing archive sections for the brain bank collection – and the second for thick sections. The "thin section" protocol was improved from a protocol used previously by us (Grinberg et al., 2009a). The celloidin was removed by immersing the sections in a 1:1 ether–100% ethanol solution for 2 min.

2.2.5.1. Immunoperoxidase protocol for thin sections. After having the celloidin removed, sections were hydrated, immersed in methylsalicylate for 1 h and embedded in Paraplast plus (Leica Microsystems, Buffalo Grove, IL), a low melting-point paraffin. Each section was then placed between two filter papers and pressed between histological cassettes to ensure flatness. These paraffin blocks were cut into 4–20 μm sections using a rotation microtome (HM355S, Thermo Scientific, Waltham, MA, USA) and mounted on Superfrost Plus Gold Microscope Slides. We optimized immunohistochemistry reactions for several antibodies of interest (Table 2) using as starting point the protocols already in use at the UCSF brain bank for paraffin-embedding sections. Briefly, sections were mounted on slides and non-specific binding was blocked by incubation in methanol with 3% H_2O_2 for 15 min, followed by 3× 5 min washes in phosphate-buffered saline (PBS) and antigen retrieval by autoclaving at 105 °C for 5 min in 0.1 M citrate buffer (pH 6.0). Subsequently, non-specific binding sites were blocked using 5% fat free milk powder dissolved in PBS for 30 min. Sections were then incubated with the primary antibody overnight at 4 °C. Secondary biotinylated antibodies (BA1000 or BA2000, Vector, Burlingame, CA, USA) were incubated with the sections for 30 min at a concentration of 1:200. Primary and secondary antibodies were diluted in 5% milk/PBS solution. Immunoreactivity was detected by incubation with an avidin–biotin complex (Vectastain ABC Kit, Vector, Burlingame, CA, USA) for 30 min followed by exposure to the chromogen diaminobenzidine tetrahydrochloride 3,3 (ImmPACT DAB Peroxidase Substrate, Vector, Burlingame, CA, USA). Sections were then submitted to 3× 5 min washes in PBS between each incubation step. Positive and negative tissue controls sections were routinely included for quality control purposes. Finally, all sections were counterstained with hematoxylin and mounted on glass slides using synthetic resin. Because beta-amyloid is detected in the brainstem only in AD late stages and alpha-synuclein is a marker of Parkinson's disease rather than AD, we optimized the immunohistochemistry protocol for these two markers using an additional subject. The midbrain of this 78-year-old male that showed both severe AD and Parkinson's disease was processed exactly like the other four cases.

2.2.5.2. Immunoperoxidase protocol for thick sections. After celloidin removal, the sections were submitted to the same immunostaining steps described in Section 2.2.5.1, but in free-floating condition. Incubation time was doubled to allow proper solution penetration into the tissue (Table 2). After immunostaining, the sections were submitted to an optical clearing protocol as described in Erturk et al. (2012) to facilitate deep tissue imaging. Briefly, sections were cleared in 50%, 70%, 80% (v/v) tetrahydrofuran (THF; Sigma–Aldrich, St. Louis, MO, USA) in distilled water for 1 h each, followed by two 1 h washes in 100% THF. Sections were

Table 2
Antibodies optimized in this study. Adopted dilution was the same for paraffin-embedded human tissue previously embedded in celloidin and celloidin embedding tissue.

Antibodies	Source	Use	Dilution
LB509	Invitrogen, CA	Detection of alpha-synuclein (Lewy bodies and neurites)	1:500
C92-605	BD Biosciences, CA	Detection of the active caspase-3	1:250
CP13	Gift from Prof. Davies, New York, NY	Detection of phosphorylated tau protein (neurofibrillary tangles)	1:500
4G8	Covance, Princeton, NJ	Detection of β-amyloid (plaques)	1:2000
PH8	Millipore, Billerica, MA	Detection of phenylalanine hydroxylase (positive on dorsal raphe nucleus)	1:500
TH	Sigma, St Louis, MO	Detection of tyrosine hydroxylase (positive on substantia nigra and locus coeruleus)	1:500
TDP-43	ProteinTech Group, Chicago, IL	Detection of normal and abnormal TDP-43 protein	1:500

than submerged in dichloromethane and dibenzyl ether (both from Sigma–Aldrich, St. Louis, MO, USA) for 45 min and 1 h respectively, on a shaker set at high speed to ensure uniform clearing. Following the DBE step, sections became transparent and were subsequently mounted on glass slides using a toluene-based mounting medium (Thermo Scientific, Waltham, MA, USA).

2.2.5.3. Double immunofluorescence staining. Thin sections obtained as described in Section 2.2.5.1 were autoclaved and blocked with 0.1% Sudan black B (Sigma–Aldrich, St. Louis, MO, USA) dissolved in 70% alcohol for 20 min to quench autofluorescence. Non-specific binding sites were subsequently blocked with 1% bovine serum albumin (BSA) and 2% goat (NG) serum in PBS with 0.02% Tween-20 for 30 min. Sections were incubated with primary antibodies overnight at 4 °C in blocking solution (Table 2), followed by incubation with the corresponding fluorescent secondary antibodies for 1 h at room temperature (1:100; DyLight 488 Horse Anti-Mouse (Vector Labs, Burlingame, CA, USA), 1:100; Alexa Fluor 568 Goat Anti-Mouse (Invitrogen, Grand Island, NY, USA), DyLight 549 Goat Anti-Rabbit (Vector Labs, Burlingame, CA, USA)). Neuronal cell bodies were labeled with Neurotrace 435/455 for 30 min (1:50; Life Technologies, Grand Island, NY, USA). Reactions in which both primary antibodies were raised against mouse, for instance CP-13 and TH or CP13 and PH8, were carried out in two steps. Each primary antibody was incubated and conjugated in separate steps, with an additional blocking with BSA/NG, followed by 1:100 Goat Anti-Mouse monovalent Fab (Jackson Labs, Bar Harbor, ME, USA) between the two incubations to avoid cross-reactions. Sections were mounted on glass slides using Vectashield HardSet mounting medium (Vector Labs, Burlingame, CA, USA) and visualized with a Nikon Eclipse Ti-E widefield epifluorescence microscope using a Plan Apo 40×/0.95 oil objective (Nikon, Tokyo, Japan). 3D images were obtained with a Nikon Eclipse C1si confocal microscope equipped with 405 nm diode, 488 nm Ar-ion and 561 nm DPSS lasers, using a Plan Fluor 40×/1.30 Oil objective (all from Nikon). Images were analyzed using NIS-Elements 4.12 Nikon software. As a negative control, one brain section from each region was processed analogously to the original protocol except that PBS replaced the primary antibodies.

2.3. Tissue analysis

2.3.1. 3D reconstruction of the histological volume

All images acquired during the block sectioning were preprocessed using Adobe Photoshop CS6 (Adobe System Inc., San Jose, CA, USA) to improve contrast. The pictures were then imported to the 3D reconstruction software (Amira 5.2, Mercury Computer Systems Inc., Chelmsford, MA, USA), which converted all the outlines into digital coordinates for generation of a 3D surface representation. The profiles of the brainstem and individual nuclei of interest were traced semi-automatically on the digital pictures using a graphic tablet (Bamboo, Wacom, Vancouver, Canada). Brainstem's boundaries were determined directly on the digitalized picture thanks to the contrast between the embedding media and the tissue created by addition of Sudan black B (Fig. 2D). Region of interest (ROI) boundaries were determined on the gallocyanine-stained sections using a stereomicroscope (RZ-10BD100/B765, Meiji Techno, Saitama, Japan) and were identical for stereology and 3D reconstructions. Surface area and volume of the reconstructed objects were calculated by the software. This method has been used by us and others and has been described in detail elsewhere (Dacosta et al., 2007; Grinberg and Heinsen, 2007; Heinsen et al., 2004; Neusser et al., 2006).

Table 3
Sampling parameters for stereological analysis.

	Total markers counted	Number of sections	Number of sampling sites	User defined mounted thickness	Estimated population using user defined section thickness	Coefficient of Error (Gundersen), $m = 1$	Coefficient of error (Schmitz–Hof)	Counting frame area (XY) (μm^2)	Sampling grid area (XY) (μm^2)
Locus coeruleus analysis									
Pilot case 1 oversampled	1771	24	512	290.0	55,607.50	0.02	0.024	13,828.1	67,374.0
Pilot case 1 resampled	304	24	78	290.0	59,721.59	0.06	0.057	13,827.4	421,515.0
Case 2	547	24	90	290.0	107,459.58	0.04	0.043	13,827.4	421,515.0
Case 3	702	18	83	290.0	137,909.72	0.04	0.038	13,827.4	421,515.0
Case 4	373	22	69	290.0	73,276.82	0.05	0.052	13,827.4	421,515.0
Case 5	267	20	66	290.0	52,413.77	0.06	0.061	13,827.4	421,515.0
Dorsal raphe nucleus analysis									
Pilot case 2 oversampled	4941	26	695	290.0	155,142.13	0.02	0.014	13,828.1	67,374.0
Pilot case 2 resampled	3051	26	673	290.0	143,697.20	0.02	0.018	13,828.1	67,374.0

2.3.2. Stereological analyses

Stereological analyses were performed using the StereoInvestigator set-up (MBF StereoInvestigator v.10, MBF Bioscience, Williston, VT, USA), which consisted of a motorized stage system, a bright field microscope (Axio A2, Zeiss Microscopy, Thornwood, NY, USA) and a color camera (1600 H × 1200 V picture elements native output, 1.92 megapixel; QImaging, Surrey, Canada) connected to the software. ROI boundaries were traced in low magnification using an EC-Plan Neofluar 5×/0.16 objective. Cells were counted in high magnification with a Plan-Apochromat 40×/1.30 oil objective (both objectives from Zeiss Microscopy). The optimal parameters for estimating neuronal numbers using the Optical Fractionator probe were derived from a 'Resample–Oversample' analysis probe included in the StereoInvestigator software (Slomianka and West, 2005). We used case #1 for the locus coeruleus and case #3 for dorsal raphe nucleus (Table 1). The pilot studies aimed to determine the minimum amount of sampling and counting necessary to achieve the desired precision of sampling.

The dorsal raphe nucleus was identified using the Atlas of the Cytoarchitecture of the Human Brain Stem complemented by a more recent cytoarchitectonics paper by Baker et al. (Baker et al., 1990; Olszewski and Baxter, 1982). The locus coeruleus was identified using the Atlas of the Cytoarchitecture of the Human Brain Stem (Olszewski and Baxter, 1982). Parameters for neuronal estimates of the substantia nigra and nucleus basalis of Meynert were optimized as a part of other studies (data not shown; Grinberg and Heinsen, 2007).

The nucleolus was used as the representative cell feature for neuronal quantification. All even-numbered gallocyanine-stained sections crossing the ROIs were used. This resulted to a section interval of 2 that remained consistent in all cases. The dorsal raphe nucleus was analyzed bilaterally, while locus coeruleus was analyzed unilaterally to increase time efficiency.

The initial oversample parameters were set for generating at least 10 counting frames per section for each ROI. The grid size was automatically generated. The optical fractionator top guard zone was established as 20 μm and disector height at 90 μm, based on the minimum section thickness. The results were plotted into graphics that generated a mean population estimate as the section interval and disector spacing were increased. The ROIs were recounted (resampled) using optimal parameters derived from the data plotted in the resample-oversample graphs. Optical estimation of our thick sections thickness was limited by the restricted working distance of the high magnification lens available in the marker. Therefore, section thickness was determined as the average of measurements in three different regions of each section. Measurements were taken with a calibrated caliper with a resolution of 0.01 mm and accuracy of 0.02 mm, right after the final xylene treatment before mounting. Both Gundersen's and Schmitz–Hof's coefficient of error (CE) of the total number of neurons were evaluated using the prediction methods included in the StereoInvestigator software (Gundersen et al., 1999; Schmitz, 1998)(Table 3).

3. Results

Fig. 4 summarizes the protocol steps.

3.1. Tissue processing

3.1.1. Celloidin embedding

A pressure of −600 mb (−60 kPa) in the desiccator hardened the blocks in two days and did not cause tissue displacement or small vessel rupture. At this pressure, celloidin did not penetrate the tissue, but rather surrounded it tightly. It resulted in a smooth block for cutting. On the other hand, the block exposed to a pressure of −400 mb took one week to harden. The longer hardening time resulted in celloidin penetrating the tissue and causing distortion.

3.1.2. Sectioning and photographing the celloidin block

Two blocks were sectioned on the rotation microtome and the other two in the sliding microtome (Figs. 1 and 3). Section thickness was controlled with a sensitive caliper and remained accurate and constant throughout the sectioning on both microtomes with less than 3% variation. The sliding microtome was equipped with an extra-long blade (8 in., 20 cm) and allowed for accommodation

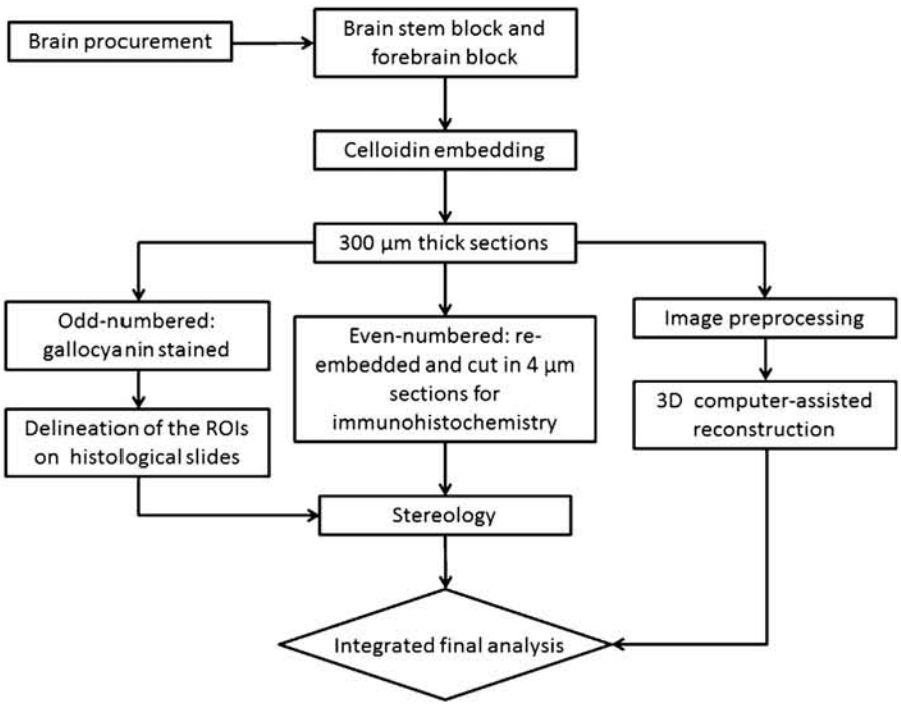

Fig. 4. Workflow diagram of the major steps of the optimized protocol.

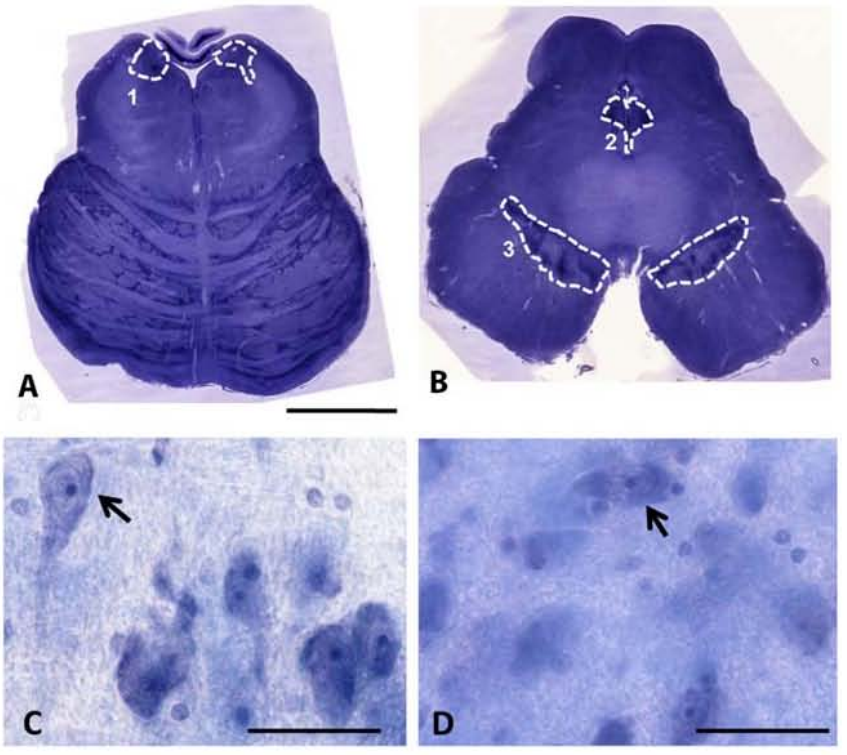

Fig. 5. Gallocyanin staining of 300 μm-thick brainstem sections: in upper row, sections were stained with gallocyanin at the level of the pons (A) and midbrain (B). Note how the combination of this staining and the high tissue thickness results in great cytoarchitectonic resolution at naked eye. The traced areas indicate the isodendritic core nuclei. In lower row, gallocyanin stained raphe nucleus was visualized at high magnification. (C) shows a slide submitted to protocol A. Note the well-defined nucleoli with minimal background, in contrast to image D where the background is dark and nuclei not readily identifiable (protocol B). Scale bars: upper row – 1 cm and lower row – 10 μm. 1: locus coeruleous/sub-coeruleous complex. 2: Dorsal raphe nucleus. 3: Substantial nigra.

of larger blocks (such as the forebrain). In addition, the position of the block holder permitted the camera to be mounted in a position without obstructing the operator view (Fig. 3B). The rotation microtome was appropriate for cutting small blocks, but due to the cutting angle, a camera mounted in an orthogonal position obstructed the operator.

3.1.3. Gallocyanine staining

Protocol A (2 h, 4% Tween 20) produced better gallocyanine staining than protocol B (2 h, 2% Tween 20), as the cell nuclei were clearly visible and the myelin was preserved, with minimal background staining. Protocol B resulted in blurred images with more diffuse cell staining (Fig. 5).

3.1.4. Immunohistochemistry

Immunohistochemistry on thick sections did not warranted any complications. The optical clearing process turned the tissue background transparent and resulted in an excellent optical resolution (Fig. 6A and B). Transforming 300 μm thick sections into thinner sections proved to be challenging. In order to produce the required number of thinner full-face sections, the thicker section has to lie absolutely flat in the paraffin block. Following several trials, we finally succeeded using large embedding metal molds and a flat metal stamp to press the sections at the bottom of the mold during paraffin hardening. The vault caused by the metal device was later filled with paraffin. Smaller regions such as medulla oblongata could then be cut into full face 4–20 μm thick sections, whereas larger specimens, such as the midbrain, could be cut at a maximum thickness of 8 μm to guarantee a minimum set of five full face slides required by the UCSF brain bank diagnosis protocol (Fig. 6C).

The optimal concentrations for the antibodies tested are described in Table 2 and results depicted in Fig. 7.

3.1.5. Immunofluorescence

Double immunofluorescence staining, CP-13/PH8 and CP-13/TH counterstained with Neurotrace resulted in excellent discrimination of the proteins of interest with subcellular resolution (Figs. 8 and 9). Neurotrace is superior to DAPI for our purposes because of its Nissl staining properties, suitable for identifying nucleoli and neuronal body profiles.

3.2. Tissue analysis

3.2.1. Stereology

The 300 μm thick gallocyanine-stained sections fulfilled all the requirements for unbiased design-based stereology. All cells within each ROI had equal change to be selected for counting, since (1) the whole structure was embedded in celloidin and sectioned serially; (2) ROI boundaries were easily recognizable due to the high tissue thickness and use of gallocyanine staining. Gallocyanine penetrates into the whole tissue thickness, providing a sharp nucleolus staining with a low background, and; (3) high section thickness created the three-dimensional design required by the optical fractionator, making the estimates independent of the size, shape, spatial orientation, and spatial distribution of the neurons within the ROI.

The average *Z*-axis (height) shrinkage was 290 μm (3.3%). Based on the resample-oversample graphs for the locus coeruleus (Fig. 9), the 6th sampling site was chosen as the optimal interval spacing in the sampling grid. The total neuron population estimate for the locus coeruleus was 55.607 cells (CE-Gundersen = 0.02 and CE-Schmitz and Hof = 0.024) using the oversample parameters and

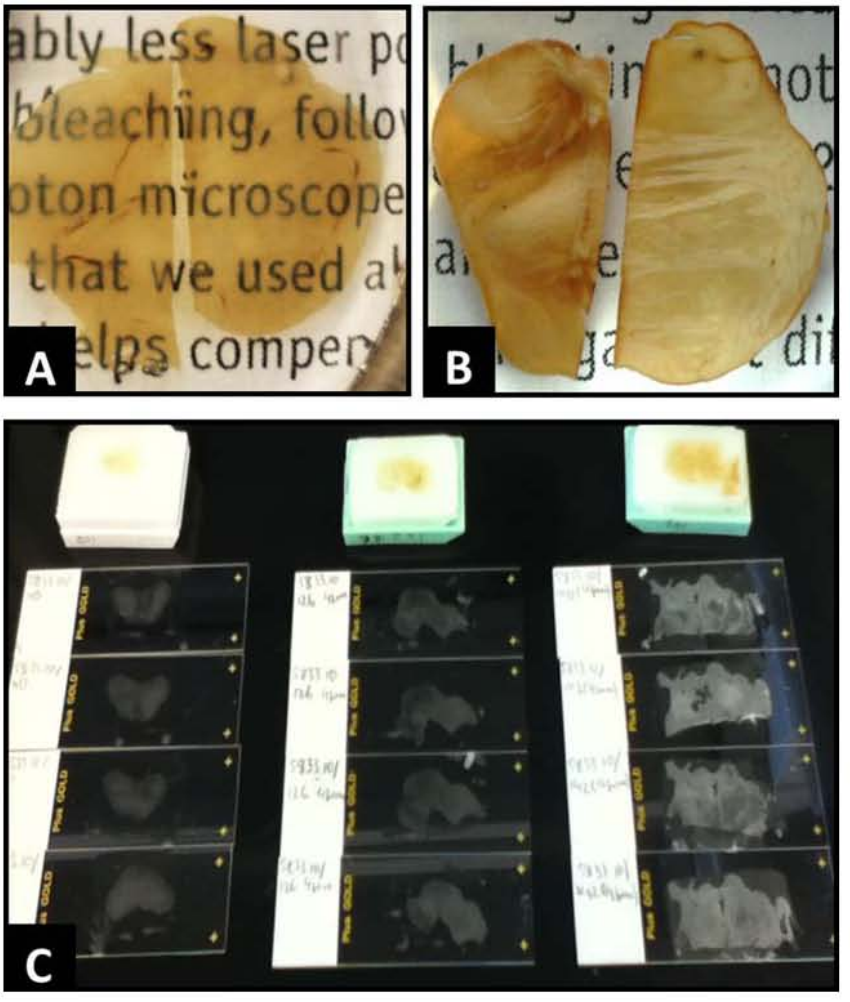

Fig. 6. Processing of 300 μm thick brainstem sections. After immunostaining, thick sections were submitted (A) or not (B) to an optical clearing protocol for lipid removal (Erturk et al., 2012). The optical transparency of the lipid-free tissue can be easily appreciated by the clearly visible background. (A and B) Both sections underwent immunohistochemistry for PH8 (midbrain; left) or TH (pons; right). (C) Thin (4 μm) histological sections were produced from celloidin-embedded histological sections re-embedded in paraffin. We successfully generated several full-faced sections from small medulla oblongata blocks (on the left) to large midbrain blocks (on the right).

59.721 cells (CE-Gundersen = 0.06 and CE-Schmitz and Hof = 0.057) using the resample parameters (Table 3). We have successfully used the above parameters for estimating the locus coeruleus neuronal population of case #1 and four additional cases and obtained a range of 52.414–137.910 neurons, with a high precision CE range (Table 3).

For the dorsal raphe nucleus, a smaller disector interval (2.25) was chosen based on the resample-oversample study (Fig. 10; Table 3). Interesting, the resample estimates using these parameters were almost 25% higher than the oversample estimates, without significant changes in the coefficient of error −155,142 cells (CE-Gundersen = 0.02 and CE-Schmitz and Hof = 0.014) and 206,569 cells (CE-Gundersen = 0.02 and CE-Schmitz and Hof = 0.019) for the oversample and resample analyses, respectively. We hypothesized that the discrepancy between the estimates could be due to a high neuronal anisotropy on the dorsal raphe nucleus. Consequently, we recounted the dorsal raphe nucleus neurons using the same disector spacing set for the oversample estimate, but shortened the disector height (60 μm). Using these adjusted parameters we estimated a total of 143,697 cells (Table 3).

3.2.2. 3D reconstructions

Sudan black B darkened the celloidin block, without penetrating into the tissue, making it an excellent tool for enhancing the contrast between tissue boundary and celloidin. This excellent contrast created the foundation for automating the 3D reconstruction of the histological volume.

Brainstem surface reconstruction consumed less than one day of work, as opposed to three days when using celloidin without Sudan black B. Reconstruction of individual nuclei took from one to four days (Fig. 11). Each ROI posed challenges for border delineation to some extent, including the medial aspect of SN due to its overlapping with ventral tegmental area, the ventrolateral aspect of locus coeruleus due to its overlapping with sub-coeruleus nucleus and the dorsolateral aspects of the dorsal raphe nucleus. Parallel immunostained sections were used to minimize possible delineation errors.

4. Discussion

In this paper, we have described an improved protocol to perform integrative network analysis of AD-related dual-nature changes combining stereology, immunohistochemistry and 3D reconstruction. We used the human brainstem in AD as a model because of our research focus on early AD stages. Nevertheless the proposed approach can be easily adapted for the study of any neurodegenerative disease in humans or in animal models, since all neurodegenerative diseases share the common features

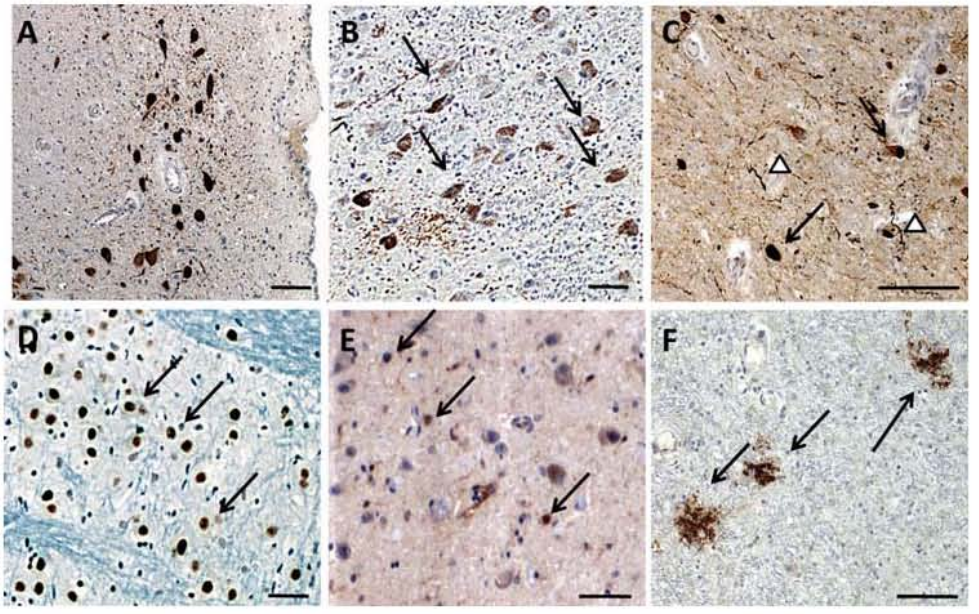

Fig. 7. Horizontal sections across the brainstem's isodendritic core nuclei from a 62 years old male at early AD stages (Braak II; A, B, D, and E) and a 78 year old male with severe AD and Lewy body disease (C and F), after immunostaining. The sections had the celloidin removed, were re-embedded in paraffin and sectioned at 4 μm thickness. (A) Midbrain section showing dorsal raphe neurons positive for PH8 (brown DAB staining). (B) Pons section immunostained with CP-13 showing phosphor-tau in locus coeruleus neurons (arrows). (C) Midbrain immunostained for α-synuclein. The arrows point to Lewy bodies and the arrowheads to Lewy neurites in the substantia nigra. (D) Pons section immunostained for TDP-43 displaying pontine neurons with nuclear TDP-43 positivity (arrows). Normal neuronal cells show nuclear TDP-43, whereas TDP-43 signal is observed in the cytoplasm of cells affected by TDP-43 proteinopathies. (E) Activated caspase-3 positivity (C92-605) in dorsal raphe neurons (arrows). Note that these neurons exhibit apoptosis-related typical nuclear shrinkage. (F) Midbrain section stained for β-amyloid. The arrows point senile plaques in the tectum. Scale bars represent 100 μm in A, B, C, D, E and 250 μm in F.

of neuronal loss and abnormal protein accumulation (Duyckaerts et al., 2009; Gómez-Isla et al., 1996). Several steps of the research protocol employed have been used in previous studies by our research group and others (Casanova et al., 2006; Grinberg et al., 2008a,b; Grinberg and Heinsen, 2007; Ravid and Grinberg, 2008; Heinsen et al., 2000; Kreczmanski et al., 2005; Schmitz et al., 2000). However, the present study devised and tested a systemized strategy to combine and harmonize all these steps. One of the main advantages of this approach is that several elements of the same network were processed together for combined analysis. This is particularly advantageous for human studies due to the human brain high inter-individual variability in size, cell number and reaction to injury. Therefore, comparisons between different brain areas should be done using data from the same subjects.

Our protocol also incorporated some additional methodologies: (1) the use of double-labeled immunofluorescence enabled us to characterize which neuron types were more vulnerable to tau-positive changes within a region of interest (ROI). Interestingly, we observed a significant number of tangles in TH- and PH8-negative neurons (Fig. 8). A large number of previous AD brainstem studies relied on TH and PH8 immunostaining for estimation of cell numbers, and thus may have underestimated the disease burden; (2) we replaced DAPI for Neurotrace as a background stain. Neurotrace works as a Nissl staining and highlight the nucleolus, an essential step for unbiased stereological estimates; (3) we optimized a recently described optical clearing method for use with celloidin-embedded sections (Erturk et al., 2012). This defatting process cleared the background and made it easier to identify neurons throughout the *Z*-axis; (4) the addition of Sudan black B to enhance

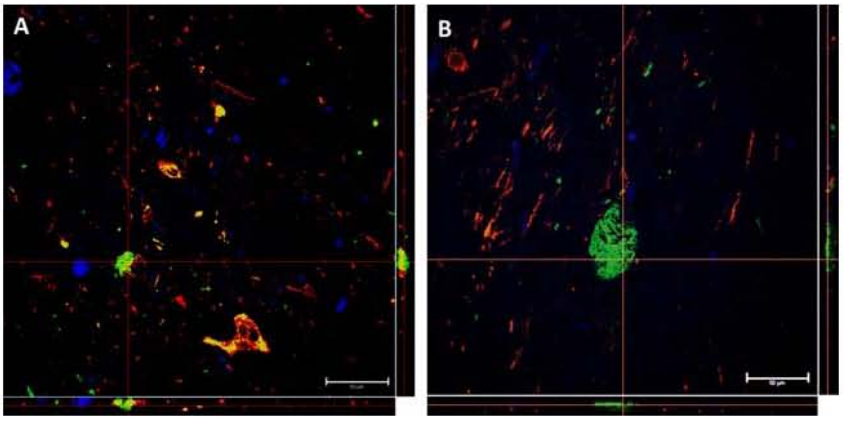

Fig. 8. Immunofluorescence staining for CP-13 (phospho-tau) and TH (tyrosine hydroxylase), counterstained with Neurotrace blue, was used to detect selective vulnerability to tau pathology according to neuronal type in substantia nigra. CP-13 positive inclusions (green, all panels) co-localized both with dopaminergic neurons (TH staining, red, all panels) (A) and non-dopaminergic cells (B). Nikon Ti-E Microscope equipped wih Yokagawa CSU22 spinning disk confocal. (For interpretation of the references to color in this figure legend, the reader is referred to the web version of the article.)

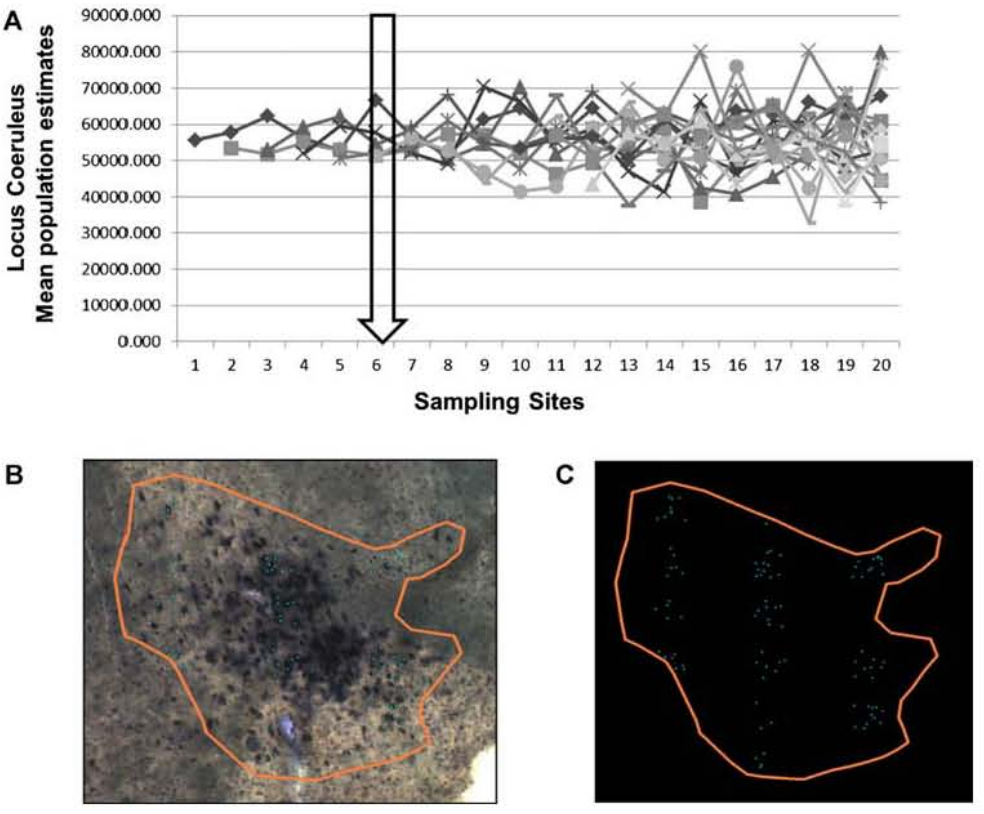

Fig. 9. Stereological estimates of the neuronal population in locus coeruleus. To establish the optimal parameters for locus coeruleus neuronal population analysis, we conducted a pilot study where the ROI was oversampled, followed by a resample–oversample analysis, represented by graph A. Based on the graphic, the same specimen was resampled using a 6.25× larger than the original (arrow; panel A). The ROI borders were identical in both disector analysis (orange contour; panels B and C). Green dots (C) represent the counted neurons within the sampling sites. (For interpretation of the references to color in this figure legend, the reader is referred to the web version of the article.)

contrast between the embedding medium and the tissue allowed for complete automation of part of the 3D reconstruction process, which was one of the most labor-intensive parts of the protocol. In fact, these innovations increased processing speed significantly and lowered processing costs, as less human power was required. This makes the approach described here feasible and affordable to a higher number of research groups, who are now able to perform morphological network analysis in a higher number of subjects within a research cycle, without compromising quality or accuracy.

Several previous investigations attempting to understand the association between neuronal loss and protein accumulation burden in AD were limited by the use of counting methods that later proved to be subjected to unacceptable bias, or by the use of unsuitable material, such as just a single thin section retrieved from archived material, per case. Neuronal estimates based on a low number of thin histological sections are likely to be biased as they may not be representative of the region as a whole. On the other hand, the small number of previous studies utilizing unbiased methods undeniably contributed to the elucidation of AD characteristics (Giannakopoulos et al., 2003, 2007; Von Gunten et al., 2005). However, even these unbiased studies were subject to certain limitations caused by the extremely complicated and time consuming protocols involved, such as a small sample number or a focus on one specific ROI. We took all these limiting factors experienced by previous studies into consideration when optimizing the approach employed in the present study.

Design-based stereology using the optical fractionator probe is the method of choice for estimating cell numbers in neuroscience, since it is considered unbiased and is able to detect even subtle group differences (Schmitz and Hof, 2005, 2007). This probe requires four prerequisites in order to minimize sampling bias: (1) all tissue slices encompassing the ROI should be available for counting. If the same slice thickness used for stereological studies in animals were adopted (20–40 μm), the number of sections per ROI would be unmanageable. For example, for processing a single human locus coeruleus, 750 μm × 20 μm thick sections or 375 μm × 40 μm sections would be necessary. We have overcome this problem by embedding the brains in celloidin and sectioning the blocks at 300 μm thickness. Celloidin was the method of choice for whole brain embedding in the past. However, this approach was almost abandoned because of its shortcomings, such as the long embedding period of up to 1 year in some cases. We employed the modified celloidin method developed by Heinsen et al. (2000), which shortened the embedding time to 3 weeks. This facilitated production of thicker slides, not possible with paraffin because of its brittleness. In addition, celloidin embedding resulted in less tissue shrinkage (10% in average on the Z axis vs. up to 70% seen in paraffin embedded tissue) (Kretschmann et al., 1982) and less deformation. Although the optical fractionator probe is not directly affected by tissue shrinkage, tissue deformation hampers analyses of the subtle sub-regional changes, very commonly seen in neurodegenerative diseases, and alters the natural relative neuronal distribution, resulting in an altered cell density distribution along the section axis (Gardella et al., 2003); (2) Tissue sections have to be thick enough to allow the use of 3D probes. We used 300 μm thick sections to fulfill this requirement; (3) The staining method should label all target cells. Nissl staining is a classic nucleic acid staining method which is often used for neuron counting because it clearly identifies cell nuclei, which are used as reference objects for the optical fractionator probe (Schmitz and Hof, 2007). We used gallocyanine as the principal dye, due to its progressive

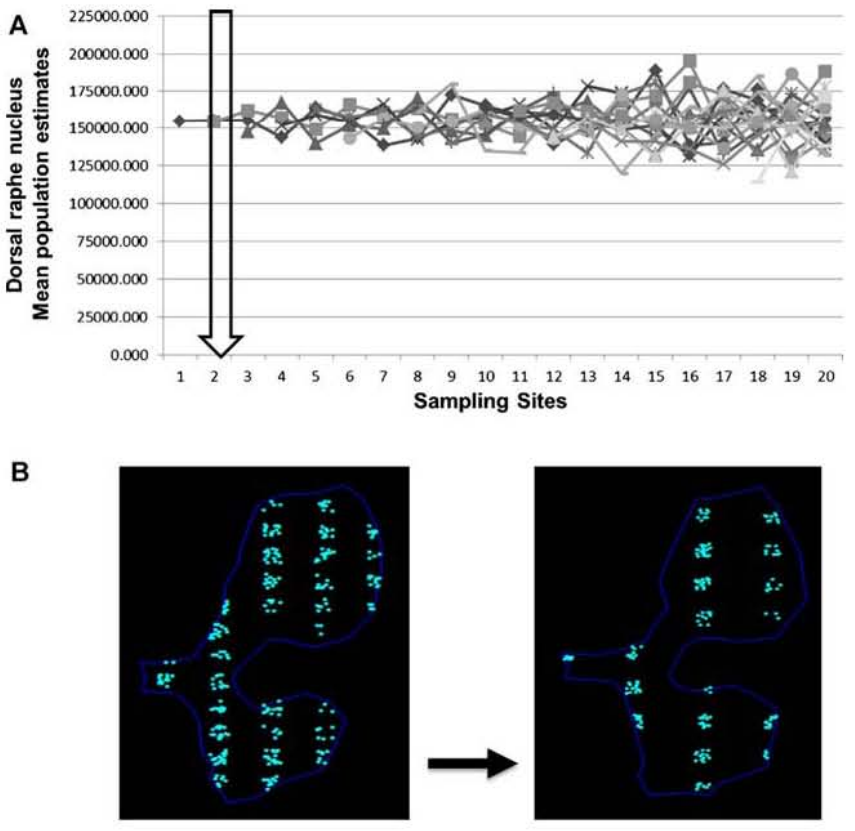

Fig. 10. Pilot study analysis for the dorsal raphe nucleus. Following the oversample–resample analysis (A), a 2.25 disector spacing was chosen as the optimal resampling parameter. The distribution of the sampling grid is shown in B, with the oversample parameters on the left and the resampling parameters on the right. Despite the low coefficient of error (CEs), the dorsal raphe nucleus neuronal population estimates showed a difference of over 25% between the oversample and resample estimates, possibly due to high heterogeneity of the cell distribution in the ROI. To overcome this discrepancy and increase our sampling precision, we successfully applied the same sampling parameters as the oversample study and decreased the disector height for time efficiency.

staining properties and consequent homogeneous staining within and across sections (Heinsen and Heinsen, 1991). In addition, gallocyanine penetrated throughout the whole tissue thickness and provided excellent cytoarchitectonic boundary recognition, an essential requirement for unbiased stereology (Heinsen et al., 2000). (4) Sections must be sampled for counting in a systematic random way. This was achieved with the aid of specialized counting software.

Due to the worldwide shortage of well-characterized post-mortem brain tissue for research, brain banks tend to maximize

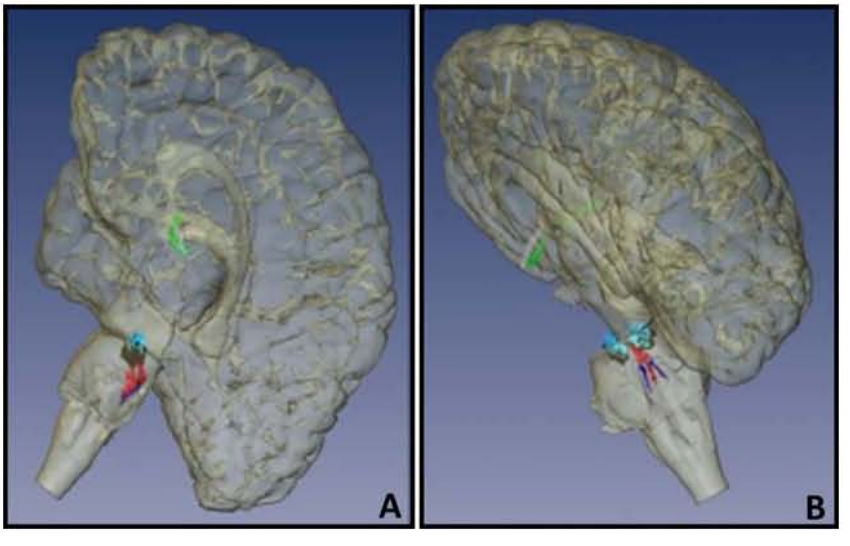

Fig. 11. 3D reconstruction of the isodendritic core. This figure shows a reconstruction of the isodendritic core components, made from serial sections using Amira: dorsal nucleus of the raphe (red), locus coeruleus (dark blue), substantia nigra (pars compacta in black and pars diffusa in light blue), and the telencephalic cholinergic nucleus basalis of Meynert (green). The components of this network share morphological features, such as neurons with big somata, overlapping dendritic fields, predominantly poorly myelinated axons that extend to distant projection sites, and aminergic/cholinergic volume transmission. (A) Medial view and (B) dorsomedial view. (For interpretation of the references to color in this figure legend, the reader is referred to the web version of the article.)

the reach of their collection, distributing tissue to a large number of investigators. In addition, neuropathological characterization requires extensive brain sampling which uses some of the available tissue. Taken together, these facts make it almost impossible for investigators to have access to brain blocks comprising an entire ROI, not to mention whole networks of interest. This means that unbiased stereological studies are often unattainable. We developed a step in our approach to guarantee that cases employed in our studies fulfill our requirements, whilst at the same time not interfering with the protocols of the source brain banks. We took advantage of the 3D reconstruction of the histological volumes to locate the ROIs required by the Brain bank diagnostic procedure. These unstained sections were re-embedded in low melting-point paraffin and sectioned into thin slices, accordingly to brain bank protocols. This was probably the most challenging step in the protocol because the 300 μm thick sections did not have enough margin for trimming and adjustment to guarantee generation of full face thin sections, and this step required considerable time and a skillful, well-trained operator. Immunohistochemistry with the most widely used antibodies in neurodegenerative diseases was carried out successfully in these thin sections. Perl et al. (2000) suggested a different approach for generating histological slides for brain banking without compromising stereological studies. This latter approach is less cumbersome than the one suggested here. However, it is not suitable for our needs due to the small size of our ROIs.

Finally, in order to understand the relationship between our ROIs and to visualize inter-subject shape differences, we reconstructed the ROIs from histological section profiles using graphic computer software (Grinberg and Heinsen, 2007; Heinsen et al., 2004). The advantages of our approach go beyond the aims of our studies. Advances in imaging, especially high definition MRI, are revolutionizing the study of neurodegenerative diseases. However, MRI maximum spatial resolution is still far worse from the subcellular resolution obtained by microscopic examination. This lack of resolution is precluding MRI to be more broadly adopted in the clinical practice. Data generated using the present approach can be co-registered with the corresponding MRI to validate MRI signal.

5. Conclusion

The present study presents an integrative method to study the range of changes seen in human neurodegenerative disease, allowing different ROIs to be studied simultaneously in the same subject. This approach can be adopted by neuropathology labs without requiring a high level of investment in new equipment. Neurodegenerative diseases display complex pathogenesis and our approach allows the study of several cases within a realistic research cycle. Although this study was performed in human brainstem, but it can also be applied to the study of neurological disease characterized by positive and negative lesions, in humans and in animal models.

Acknowledgments

We thank the patients and their families for their invaluable contribution to brain aging neurodegenerative disease research, and the staff of the Sao Paulo Autopsy Service and BBBABSG for technical assistance. Funding for this study was provided by NIH (1R01AG040311), John Douglas French Alzheimer Foundation, Coordenadoria de Apoio ao Pessoal de Nivel Superior (CAPES) – Brazil, LIM-22 – Department of Pathology, University of Sao Paulo – Brazil and Hospital Israelita Albert Einstein, Sao Paulo, Brazil. Funding sources did not have influence on study design; in the collection, analysis and interpretation of data; in the writing of the report; and in the decision to submit the article for publication. We also thank Dr. Janet Johnston (i.e.) for language editing and the UCSF Nikon Imaging Center for support with microscopy.

References

Andrade-Moraes CH, Oliveira-Pinto AV, Castro-Fonseca E, da Silva CG, Guimaraes DM, Szczupak D, et al. Cell number changes in Alzheimer's disease relate to dementia, not to plaques and tangles. Brain 2013 [epub ahead of print].

Baker KG, Halliday GM, Törk I. Cytoarchitecture of the human dorsal raphe nucleus. J Comp Neurol 1990;301:147–61.

Boxer AL, Mackenzie IR, Boeve BF, Baker M, Seeley WW, Crook R, et al. Clinical, neuroimaging and neuropathological features of a new chromosome 9p-linked FTD-ALS family. J Neurol Neurosurg Psychiatry 2011;82:196–203.

Braak H, Thal DR, Ghebremedhin E, Del Tredici K. Stages of the pathologic process in Alzheimer disease: age categories from 1 to 100 years. J Neuropathol Exp Neurol 2011;70:960–9.

Casanova MF, van Kooten IAJ, Switala AE, van Engeland H, Heinsen H, Steinbusch HWM, et al. Minicolumnar abnormalities in autism. Acta Neuropathol 2006;112:287–303.

Dacosta S, Cunha CM, Simone LRL, Schrodl M. Computer-based 3-dimensional reconstruction of major organ systems of a new aeolid nudibranch subspecies, *Flabellina engeli* lucianae, from Brazil (Gastropoda: Opisthobranchia). J Mollus Stud 2007;73:339–53.

Duyckaerts C, Delatour B, Potier MC. Classification and basic pathology of Alzheimer disease. Acta Neuropathol 2009;118:5–36.

Erturk A, Becker K, Jahrling N, Mauch CP, Hojer CD, Egen JG, et al. Three-dimensional imaging of solvent-cleared organs using 3DISCO. Nat Protoc 2012;7(11):1983–95, http://dx.doi.org/10.1038/nprot.2012.119.

Ewers M, Frisoni GB, Teipel SJ, Grinberg LT, Amaro E Jr, Heinsen H, et al. Staging Alzheimer's disease progression with multimodality neuroimaging. Prog Neurobiol 2011;95(4):535–46.

Ferretti REL, Damim AE, Brucki SMD, Morillo LS, Perroco T, Campora F, et al. BBBABSG5. Post-moretem diagnosis of dementia by informant interview. Dement Neuropshycol 2010;4:138–44.

Gardella D, Hatton WJ, Rind HB, Rosen GD, von Bartheld CS. Differential tissue shrinkage and compression in the *z*-axis: implications for optical disector counting in vibratome-, plastic- and cryosections. J Neurosci Methods 2003;124:45–59.

Geula C, Nagykery N, Nicholas A, Wu CK. Cholinergic neuronal and axonal abnormalities are present early in aging and in Alzheimer disease. J Neuropathol Exp Neurol 2008;67:309–18.

Giannakopoulos P, Gold G, Kovari E, von Gunten A, Imhof A, Bouras C, et al. Assessing the cognitive impact of Alzheimer disease pathology and vascular burden in the aging brain: the Geneva experience. Acta Neuropathol 2007;113:1–12.

Giannakopoulos P, Herrmann FR, Bussiere T, Bouras C, Kovari E, Perl DP, et al. Tangle and neuron numbers, but not amyloid load, predict cognitive status in Alzheimer's disease. Neurology 2003;60:1495–500.

Gómez-Isla T, Price JL, McKeel DW, Morris JC, Growdon JH, Hyman BT. Profound loss of layer II entorhinal cortex neurons occurs in very mild Alzheimer's disease. J Neurosci 1996;16:4491–500.

Grinberg LT, Amaro E Jr, Teipel S, dos Santos DD, Pasqualucci CA, Leite RE, et al. Assessment of factors that confound MRI and neuropathological correlation of human postmortem brain tissue. Cell Tissue Bank 2008a;9:195–203.

Grinberg LT, Amaro Junior E, da Silva AV, da Silva RE, Sato JR, dos Santos DD, et al. Improved detection of incipient vascular changes by a biotechnological platform combining post mortem MRI in situ with neuropathology. J Neurol Sci 2009a;283:2–8.

Grinberg LT, Ferretti RE, Farfel JM, Leite R, Pasqualucci CA, Rosemberg S, et al. Brain bank of the Brazilian aging brain study group—a milestone reached and more than 1,600 collected brains. Cell Tissue Bank 2007;8:151–62.

Grinberg LT, Heinsen H. Computer-assisted 3D reconstruction of the human basal forebrain complex. Dement Neuropsychol 2007;1:140–6.

Grinberg LT, Rub U, Ferretti RE, Nitrini R, Farfel JM, Polichiso L, et al. The dorsal raphe nucleus shows phospho-tau neurofibrillary changes before the transentorhinal region in Alzheimer's disease. A precocious onset? Neuropathol Appl Neurobiol 2009b;35:406–16.

Grinberg LT, Amaro Junior E, Santos DD, Pachaco SP, Ferretti REL, Leite REP, et al., Brazilian Aging Brain Study Group. Improved detection of incipient vascular changes by a biotechnological platform combining post mortem MRI in situ with neuropathology. J Neurol Sci 2009c;283(1–2):2–8, http://dx.doi.org/10.1016/j.jns.2009.02.327.

Gundersen HJG, Jensen EBV, Kiêu K, Nielsen J. The efficiency of systematic sampling in stereology—reconsidered. J Microsc 1999;193:199–211.

Hebert LE, Scherr PA, Bienias JL, Bennett DA, Evans DA. Alzheimer disease in the US population: prevalence estimates using the 2000 census. Arch Neurol 2003;60:1119–22.

Heinsen H, Arzberger T, Roggendorf W, Mitrovic T. 3D reconstruction of celloidin-mounted serial sections. Acta Neuropathol 2004:374.

Heinsen H, Arzberger T, Schmitz C. Celloidin mounting (embedding without infiltration)—a new, simple and reliable method for producing serial sections of high thickness through complete human brains and its application to stereological and immunohistochemical investigations. J Chem Neuroanat 2000;20:49–59.

Heinsen H, Heinsen YL. Serial thick, frozen, gallocyanin stained sections of human central nervous system. J Histotechnol 1991;14:167–73.
Huang Y, Mucke L. Alzheimer mechanisms and therapeutic strategies. Cell 2012;148:1204–22.
Jack CR, Knopman DS, Jagust WJ, Shaw LM, Aisen PS, Weiner MW, et al. Hypothetical model of dynamic biomarkers of the Alzheimer's pathological cascade. Lancet Neurol 2010;1:119–28.
Kreczmanski P, Schmidt-Kastner R, Heinsen H, Steinbusch HW, Hof PR, Schmitz C. Stereological studies of capillary length density in the frontal cortex of schizophrenics. Acta Neuropathol 2005;109:510–8.
Kretschmann H-J, Tafesse U, Herrmann A. Different volume changes of cerebral cortex and white matter during histological preparation. Microsc Acta 1982;86:13–24.
Korczyn AD. Why have we failed to cure Alzheimer's disease? J Alzheimers Dis 2012;29:275–82.
Morris JC. The Clinical Dementia Rating (CDR): current version and scoring rules. Neurology 1993;43:2412–4.
Neusser TP, Hess M, Haszprunar G, Schrodl M. Computer-based three-dimensional reconstruction of the anatomy of *Microhedyle remanei* (Marcus, 1953), an interstitial acochlidian gastropod from Bermuda. J Morphol 2006;267:231–47.
Ohm TG, Heilmann R, Braak H. The human oral raphe system. Architectonics and neuronal types in pigment-Nissl preparations. Anat Embryol 1989;180:37–43.
Olszewski J, Baxter D. Cytoarchitecture of the human brain stem. Basel: Karger; 1982.
Parvizi J, Van Hoesen GW, Damasio A. The selective vulnerability of brainstem nuclei to Alzheimer's disease. Ann Neurol 2001;49:53–66.
Perl DP, Good PF, Bussiere T, Morrison JH, Erwin JM, Hof PR. Practical approaches to stereology in the setting of aging- and disease-related brain banks. J Chem Neuroanat 2000;20:7–19.
Ramon-Moliner E, Nauta WJ. The isodendritic core of the brain stem. J Comp Neurol 1966;126:311–35.
Ravid R, Grinberg LT. How to run a brain bank—revisited. Cell Tissue Bank 2008;9:149–50.
Sassin I, Schultz C, Thal DR, Rub U, Arai K, Braak E, et al. Evolution of Alzheimer's disease-related cytoskeletal changes in the basal nucleus of Meynert. Acta Neuropathol 2000;100:259–69.
Schmitz C. Variation of fractionator estimates and its prediction. Anat Embryol 1998;198:371–97.
Schmitz C, Dafotakis M, Heinsen H, Mugrauer K, Niesel A, Popken GJ, et al. Use of cryostat sections from snap-frozen nervous tissue for combining stereological estimates with histological, cellular, or molecular analyses on adjacent sections. J Chem Neuroanat 2000;20:21–9.
Schmitz C, Hof PR. Riddle DR, editor. Design-based stereology in brain aging research. Boca Raton (FL): CRC Press; 2007.
Schmitz C, Hof PR. Design-based stereology in neuroscience. Neuroscience 2005;130:813–31.
Seeley WW, Crawford RK, Zhou J, Miller BL, Greicius MD. Neurodegenerative diseases target large-scale human brain networks. Neuron 2009;62:42–52.
Slomianka L, West MJ. Estimators of the precision of stereological estimates: an example based on the CA1 pyramidal cell layer of rats. Neuroscience 2005;136:757–67.
Tanner CM, Gilley DW, Goetz CG. A brief screening questionnaire for parkinsonism. Ann Neurol 1990;28:267–8.
Von Gunten A, Kovari E, Rivara CB, Bouras C, Hof PR, Giannakopoulos P. Stereologic analysis of hippocampal Alzheimer's disease pathology in the oldest-old: evidence for sparing of the entorhinal cortex and CA1 field. Exp Neurol 2005;193:198–206.